

Nonequilibrium Time Reversibility with Maps and Walks

William Graham Hoover and Carol Griswold Hoover

Ruby Valley Research Institute

Highway Contract 60, Box 601

Ruby Valley, Nevada 89833 ;

Edward Ronald Smith

Faculty of Engineering

Department of Mechanical Engineering

Brunel University, London

See /VOLUMES/SSD2/SMITH/BAKER.f

Prepared for the 6 September 2021 Conference on Nonequilibrium Molecular Dynamics

(Dated: September 21, 2021)

Abstract

Time-reversible dynamical simulations of nonequilibrium systems exemplify both Loschmidt's and Zermélo's paradoxes. That is, computational time-reversible simulations invariably produce solutions consistent with the *irreversible* Second Law of Thermodynamics (Loschmidt's) as well as *periodic* in the time (Zermélo's, illustrating Poincaré recurrence). Understanding these paradoxical aspects of time-reversible systems is enhanced here by studying the simplest pair of such model systems. The first is time-reversible, but nevertheless dissipative and periodic, the piecewise-linear compressible Baker Map. The fractal properties of that two-dimensional map are mirrored by an even simpler example, the one-dimensional random walk, confined to the unit interval. As a further puzzle the two models yield ambiguities in determining the fractals' information dimensions. These puzzles, including the classical paradoxes, are reviewed and explored here. We review our investigations presented in Budapest in 1997 and end with presentday questions posed as the Snook Prize Problems in 2020 and 2021.

PACS numbers:

Keywords: Nonequilibrium Simulations, Time Reversibility, Fractals, Baker Maps, Random Walks

I. INTRODUCTION

The averages produced by molecular dynamics and Gibbs' statistical mechanics agree for "ergodic" systems, systems with a dynamics able to access all of the (q, p) coordinate-momentum states included in Gibbs' statistical averages. Ergodicity is actually a purely theoretical construct for manybody systems. The time required for a nearly complete averaging over a many-dimensional phase space grows exponentially with system size, and exceeds the age of the universe when the number of degrees of freedom is a dozen or so. On the other hand the ergodicity of few-body models can be established and studied. Two hard disks, with periodic boundary conditions is a simple example. The eight-dimensional phase space can be reduced to three (enough for chaos) by imposing symmetry and constant energy on the dynamics. A further simplification can be attained by considering maps, in which the "next" system state is a function of the "current" state of the system. The two simplest such maps are described here, the two-dimensional Baker Map and a closely-related one-dimensional Confined Random Walk.

A. Hopf's Equilibrium Baker Map $E(x,y)$

Nearly a century ago Hopf introduced his Baker Map, reminiscent of a bread baker's dough-kneading action. We construct it here in the unit square, $0 < x, y < 1$. See **Figure 1**. The mapping at the top is based on two choices for subsequent points: For a current (green) point with $x < 1/2$ we choose

$$x_{\text{new}} = 2x \text{ and } y_{\text{new}} = (y + 1)/2 ,$$

while for a current (red) point with $x > 1/2$ we choose instead

$$x_{\text{new}} = 2x - 1 \text{ and } y_{\text{new}} = y/2 .$$

Hopf's interest was "ergodic theory" and this Baker model can be proved ergodic *most* of the time.

Here "most" of the time means choosing an irrational initial condition. Rational beginnings or numerical finite-precision simulations lead promptly to fixed points instead. The fixed-point mechanism is simply the repeated doubling of the fractional part of the x coordinate. In fact **Figure 1** shows the typical fate of a numerical implementation of Hopf's

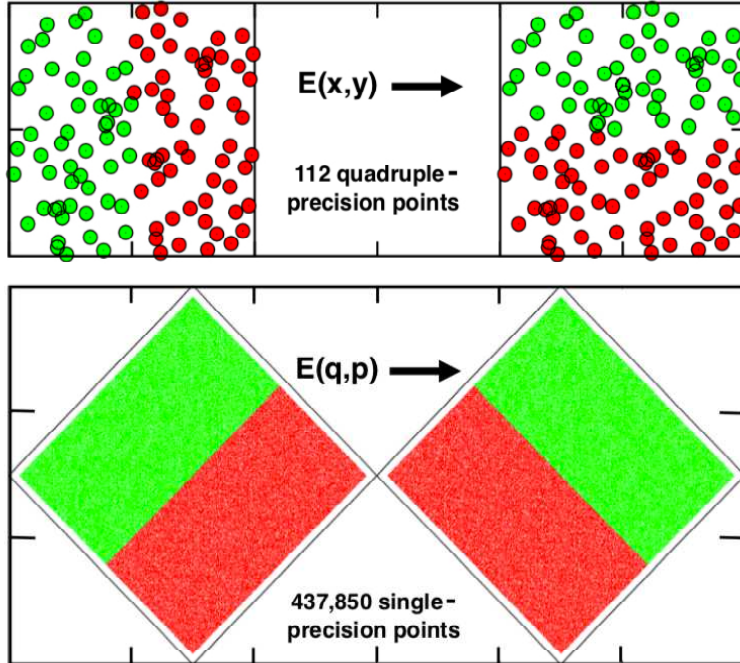


FIG. 1: Hopf’s deterministic Baker Map $E(x, y)$ maps the left/right sides of the unit square into the top/bottom halves with each iteration. The continued doubling in the x direction eventually reaches a fixed point. The Figure shows a series of 112 points generated with quadruple-precision arithmetic. Evidently Hopf could not imagine a computational implementation of his map! The diamond-shaped lower version of the map, 2×2 rather than a unit square, produces a long periodic orbit and is, unlike Hopf’s, time-reversible.

equilibrium map. The quadruple-precision simulation illustrated in the figure generates 112 (x, y) states, of which the last is a fixed point. Single and double-precision simulations likewise come to fixed-point ends, after 23 and 52 iterations of Hopf’s map. If Hopf’s evolution is instead described in terms of a rotated (q, p) coordinate system the result is a relatively long periodic orbit rather than a fixed point. Even single precision gives a period of hundreds of thousands of iterations. See again **Figure 1**.

In the summer of 1997 at the Eötvös University school/workshop meeting “Chaos and Irreversibility” Hoover and Posch¹ introduced time-reversibility and dissipation into a generalized Baker Map. Tasaki, Gilbert, and Dorfman² analyzed families of similar maps at that same meeting. See as well George Kumičák’s related work³ from 2004. Next, we focus on the specific dissipative and time-reversible (q, p) map considered by Hoover and Posch, and described in what follows.

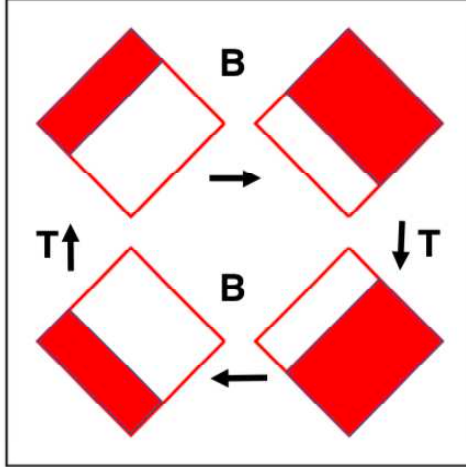


FIG. 2: The deterministic Baker Map B doubles an area $dqdp$ in the red region and halves an area in the white. The time-reversal Map T changes the sign of the vertical “momentum-like” variable p . The diamond-shaped domain of the map is $|q \pm p| < \sqrt{2}$. A counterclockwise circuit of the four states follows if B is replaced by B^{-1} as T and T^{-1} are identical.

B. From Equilibrium to Nonequilibrium with Time-Reversible Maps

Molecular dynamics is “time-reversible” if the previous step can be recovered by a three-step process: [1] At time $t + dt$ change the signs of the momenta, $\{ +p \rightarrow -p \}$; [2] Propagate the resulting reversed $(q, -p)$ state (backward) to time t ; [3] Change the signs of the momenta, matching the original $(q, +p)$ state at time t . A time-reversible Baker Map $B(q, p)$ would obey the relation $B^{-1} = T \times B \times T$, where T is the (time reversal) mapping that reverses the momenta. If we choose (q, p) coordinate-momenta variables in a 2×2 rotated Baker map, the “equilibrium” (incompressible) map E , illustrated in **Figure 1** has the analytic form

$$\text{if}(q < p) \quad q_{\text{new}} = (5/4)q - (3/4)p + 3d \quad ; \quad p_{\text{new}} = -(3/4)q + (5/4)p - d$$

$$\text{if}(q > p) \quad q_{\text{new}} = (5/4)q - (3/4)p - 3d \quad ; \quad p_{\text{new}} = -(3/4)q + (5/4)p + d$$

where $d = \text{sqrt}(1/8)$. This “motion” is analogous to ordinary Hamiltonian mechanics, where the phase volume $dqdp$ is conserved by Hamilton’s motion equations. In *nonequilibrium* molecular dynamics the extraction of heat, corresponding to entropy loss, leads to a continuous loss of phase volume. A mapping analogy can be illustrated by constructing a compressible mapping, as shown in **Figures 2 and 3**.

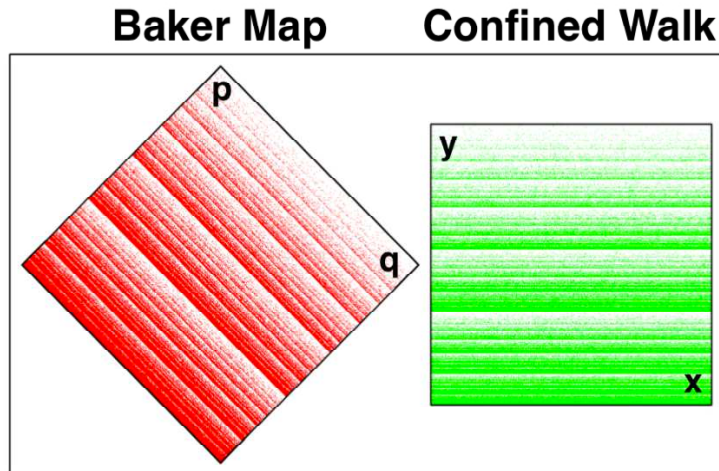


FIG. 3: One million iterations of the Baker Map and the Confined Walk are compared. A scaling and translation of the Baker Map solution at the left to the unit square replicates the solution of a stochastic confined random walk problem where x and y are stochastic variables. The walk confined to the unit interval $0 < y < 1$ is generated with a random number relating the “next” value of y to the “last”. The latter is either $y/3$ or $(1+2y)/3$, corresponding to steps to the bottom third or upper two thirds of the green million-iteration solution at the right of **Figure 3**. The (q, p) Baker Map at the left and the (x, y) Confined Walk at the right provide indistinguishable fractals when rotated 45 degrees and scaled by a factor of two, as shown in the figure. The Confined Walk shown there occupies a unit square, $0 < (x, y) < 1$. We show a 2×2 version, with $|q \pm p| < \sqrt{2} \leftrightarrow |x, y| < 1$, here to clarify the details of the fractal structure..

Nonequilibrium Molecular Dynamics has a half-century history of providing simulations of viscous and heat-conducting flows driven by boundary differences in velocity and temperature respectively^{4,5}. Stationary state simulations are typically stabilized by time-reversible thermostat forces, linear in momentum. These “thermostat forces” impose the desired thermalized boundary conditions⁶⁻⁸ to maintain nonequilibrium steady states. Such simulations are irreversible despite their time-reversible motion equations. These simulations invariably provide the positive viscosities and heat conductivities associated with Loschmidt’s paradox.

Phase-space analyses of small-scale steady-state nonequilibrium simulations indicate stable periodic steady-state structures, “attractors” in phase space. The attraction is termed “strange” because constrictive attractor dynamics simultaneously exhibits expansive Lyapunov instability, with small perturbations growing exponentially in time. Despite this expansive instability the phase volume comoving with a trajectory point is attractive, shrinking

with time as the computation settles onto a periodic, but Lyapunov unstable, orbit. This periodicity illustrates Zermélo’s recurrence paradox and implies that the actual dimensionality of computational nonequilibrium steady states is only unity. But, as the computational precision is further refined the orbit lengthens, with the length soon becoming too long to measure and with the one-dimensional trajectory defining a natural measure (or coarse-grained probability density) with a fractal information dimension in the phase space.

Thus precise long-time nonequilibrium trajectories in phase space come to define *fractal* structures, still space-filling, but only sparsely. The dimensionality of these structures is significantly less than that of the equilibrium phase space supporting their nonequilibrium dynamics. The “information dimensions” of these fractals can be estimated by phase-space binning, as we shall demonstrate. In fact such phase-space dimensionality descriptions are not completely clearcut as their description with simple models like Baker’s reveals a sobering nonuniform convergence. The simplest model flows exhibiting these interesting fractal formations are one-particle systems with three-dimensional phase spaces^{9,10}. Those spaces include a single coordinate-momentum pair along with a time-reversible friction coefficient ζ . The friction coefficients stabilize nonequilibrium steady states.

In the remainder of this work we discuss the two simplest models, a two-dimensional Baker Map and a related one-dimensional confined random walk. Their study sheds light on the coexistence of time reversibility with the dissipation typifying strange attractor structures in model phase spaces.

II. THE TIME-REVERSIBLE DISSIPATIVE BAKER MAP

Maps, as opposed to flows, can exhibit similar time-reversible dissipation while occupying only one or two phase-space dimensions. We consider here a compressible version of the “Baker Map”¹⁻³. It evolves a single coordinate-momentum pair of variables (q, p) as is illustrated in **Figure 2**. A longtime solution appears at the left in **Figure 3**. In the two-dimensional (q, p) coordinate-momentum phase space compressible Baker-Map dynamics simply generates a new (q, p) pair from the old one, as described by a linear map. At the top of **Figure 2** the smaller red area with $q - p < \sqrt{(2/9)}$ is expanded twofold by the Baker Map B. The expanding map has the analytic form:

$$q_{\text{new}} = +(11q/6) - (7p/6) + 14d ; p_{\text{new}} = -(7q/6) + (11p/6) - 10d .$$

The constant d is $\sqrt{(1/72)}$. Notice that the expanding map has a (q, p) Jacobian determinant of $(121 - 49)/36 = 2$, signalling a doubling of area with each iteration. In the larger white region the map, likewise linear, contracts:

$$q_{\text{new}} = +(11q/12) - (7p/12) - 7d ; p_{\text{new}} = -(7q/12) + (11p/12) - d .$$

Here the determinant of the contracting map is $(121 - 49)/144 = 1/2$ signifying twofold compression. **Figure 3** illustrates a million-iteration solution of the mapping equations.

Figure 2 illustrates the time-reversibility of the map. First, starting at the upper right of the figure, change the sign of the vertical “momentum variable” p with the map “T”, ending at lower right; next map forward with “B” to lower left; last reverse time again with “T” returning (q, p) to its original top left pre-mapped location, demonstrating that the inverse mapping is $B^{-1}=TBT$. This identity defines a time-reversible mapping.

Though the map looks even-handed compression invariably wins out over expansion. It must! A little reflection identifies compression with stability and expansion with its opposite, instability. An unphysical hypothetical system in which expansion wins out over compression would correspond to numerical instability with an exponential divergence of the comoving phase volume. In numerical work only about ten percent of the simple Baker-Map iterations are computationally reversible in the sense that applying the inverse mapping undoes the most recent iteration precisely so that $B^{-1}B$ leaves (q, p) unchanged.

III. IRREVERSIBILITY THROUGH SHRINKING PHASE VOLUME

An understanding of the shrinking phase volume, which leads to an apparent fractal (fractional dimensional) phase-space object is straightforward in the Baker Map example of **Figure 2**. The map, whether in the red region or the white, always expands in the northwest-southeast direction parallel to lines of constant $q+p$. This expansion characterizes Lyapunov instability, the growth of microscopic perturbations to macroscopic scale. In the perpendicular direction, parallel to lines of constant $q - p$, the map contracts to the self-similar fractal structure displayed in **Figure 3**.

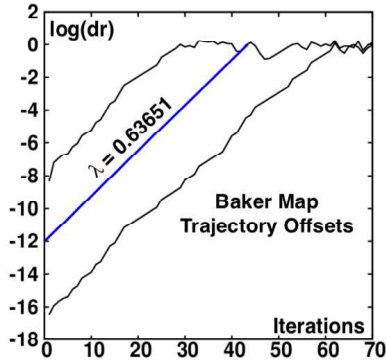


FIG. 4: Comparison of the differences $dr = \sqrt{q^2 + p^2}$ between single and double precision simulations (above) of the Baker Map and double and quadruple precision simulations (below) with all three trajectories started at the origin. The straight blue line has a slope corresponding to the largest Lyapunov exponent, $\lambda_1 = 0.63651$.

A. Lyapunov Instability and Exponential Growth

Figure 4 illustrates the exponential character of the expansive northwest-southeast growth by displaying the offset between single- and double-precision simulations, the uppermost of the three curves in the figure. Both simulation types begin at the $(q, p) = (0, 0)$ origin at the center of the diamonds shown in **Figures 1 through 3**. The initial separation immediately reflects the roundoff error of the single-precision mapping, of order 10^{-10} . The single-double separation increases by ten orders of magnitude in about 40 iterations of the map. Similarly, the double-quadruple separation likewise grows exponentially. In that more-nearly-accurate more-precise case the growth rate is the same $e^{+\lambda_1 t}$. λ_1 is the largest Lyapunov exponent. Its numerical value is 0.63651. The exponent and the blue middle line in **Figure 4** drawn with its slope corresponds to averaging the growth rates in the red and white regions, $\ln(3)$ and $\ln(3/2)$ respectively, taking into account that the white compressive region is twice as likely as the red. The result is the time-averaged expansion rate:

$$\langle \lambda_1 \rangle = (1/3) \ln(3) + (2/3) \ln(3/2) = (1/3) \ln(27/4) = 0.63651 .$$

Similarly, the compression perpendicular to the expansion gives the second Lyapunov exponent:

$$\langle \lambda_2 \rangle = (1/3) \ln(2/3) + (2/3) \ln(1/3) = (1/3) \ln(2/27) = -0.86756 .$$

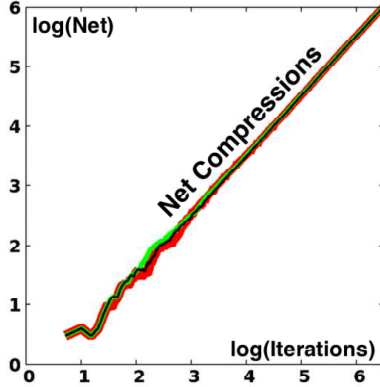


FIG. 5: Excess of compressive over expansive iterations of the single-, double-, and quadruple-precision Baker maps. The differences between them are visible between 20 and 1000 iterations of the maps. The final values of the excess are 1000742, 1000250, and 998236 for the three sets of three million iterations beginning at $(0, 0)$.

This analysis is in good agreement with the numerical data. With an initial double-precision roundoff error of order 10^{-17} the exponential loss of accuracy expands to unity after about 60 iterations of the map: $10^{+17} \simeq e^{0.63651 \times 60}$, as in the lower curve.

B. Compression with Expansion Leads to Irreversibility

Despite the exponential growth of northwest-southeast separations the overall phase volume shrinks. On average a white area is halved two thirds of the time while a red area doubles one third of the time. Thus overall the comoving area decreases as $2^{(-t/3)}$ with t iterations. That area is soon reduced to a vanishingly-small fraction of its initial value. That fraction is of order e^{-100} for a thousand iterations of the map. This contraction of area accounts for the sparse appearance of the thousands of mapped points in the smallest-scaled regions of **Figure 3**. The mean densities in the self-similar bands decrease with increasing values of y :

$$\langle \rho(0 < y < \frac{1}{3}) \rangle = 2^1 ; \langle \rho(\frac{3}{9} < y < \frac{5}{9}) \rangle = 2^0 ; \langle \rho(\frac{15}{27} < y < \frac{19}{27}) \rangle = 2^{-1} \dots .$$

The expansive “strange” portion of the mapping is responsible for this decrease in density even though it is unlikely relative to compression. Consider an initial point at the origin $(q, p) = (0, 0)$ and follow it forward in time, counting the net number of compression steps. **Figure 5** shows the results of three million iterations of the map in single, double, and

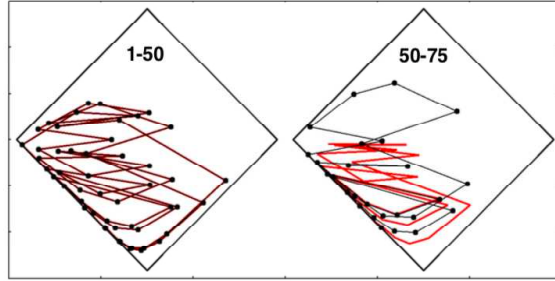


FIG. 6: 50 (at the left) and 25 additional (at the right) iterations in double (black) and quadruple (red) precision for the two-dimensional (q, p) Baker Map B with the initial point at the origin $(0, 0)$. Lyapunov instability makes the difference between the two solutions visible after about 70 iterations, as can be seen at the right.

quadruple precision. As expected the net numbers of compressive iterations are “close to” [within a thousand or so] one-third the total.

IV. POINCARÉ RECURRENCE OF THE BAKER MAPS

A fringe benefit of the diamond-shaped Baker Map is the relatively long Poincaré recurrence time. The computational “noise” contributing to this longevity can be traced to the irrational square roots in the mapping. The single-precision mapping which we have used in **Figures 4 and 5** has a periodic orbit of length just over a million iterations, 1,042,249 to be precise. The double-precision mapping settles into a periodic orbit repeating after a few trillion iterations¹¹. The (x, y) Cartesian coordinate version of the map corresponding to the orientation at the right in **Figure 3** is not well suited to computation due to its many short periodic orbits, many of which are stable (which we view as “unphysical”. A clear and comprehensive analysis of the generalized Baker Map problem (with arbitrarily small and large expansions and contractions) was presented by Kumičák in 2005³.

V. CHARACTERIZING CHAOS IN THE BAKER MAP

Numerical solutions carry a fixed number of digits, 9, 17, and 36 for single-, double-, and quadruple-precision numbers on the unit interval. Chaos is characterized by the exponential growth of small perturbations. The Baker Map’s largest Lyapunov exponent is 0.63651, so that the differences seeded by roundoff between single- and double-precision, and between

double- and quadruple-precision solutions can be estimated from **Figure 4** just as easily as from the analytic growth rates. That figure illustrates the offsets and **Figure 6** the trajectory differences between 50 and 75 iterations of the double and quadruple-precision maps. At 50 iterations, corresponding to multiplying by $e^{32} \simeq 10^{14}$, roundoff error hasn't yet amplified the difference between double and quadruple precision to visibility, while 75 iterations are more than sufficient to lose any visible correlation between the two solutions.

The right side of **Figure 3** shows that a stochastic view of the map, traceable to its chaos, is quite proper. Before the mapping shown at the top of **Figure 1** is executed we note that the white southeastern area is twice that of the northwestern red area so that compressive steps (into the highest-density lower third of the unit square) are twice as likely as expansive steps (into the upper two-thirds). The preponderance of the excess, lower - upper, is shown in **Figure 5** and approaches, on average, $t/3$ as the number of iterations t increases. We would expect the error in this statistical estimate to become visually negligible, say one percent, once the number of iterations is of order 10^4 . A look at the figure shows that the statistical bumpiness away from a straight line becomes visually negligible between 1000 and 10,000 iterations, just as one would expect for a stochastic, rather than deterministic, process.

It is an article of faith that the x motion of the (x, y) map is completely random¹². This statistical view is consistent with our numerical work so that we believe it is fully justified. It is easily checked by comparing bin populations for the Map and the Walk after millions or billions or trillions of iterations. See **Figure 7** for a million-iteration sampling of 2187 bins for both approaches. Let us consider the confined random walk problem in more detail next¹¹⁻¹³.

VI. RANDOM WALK ANALOG OF THE BAKER MAP

A random-walk analog for the progress of the Cartesian y variable on the unit interval can be modelled given current values of x and y . A new value x_{new} can be chosen at random, while y_{new} depends upon both a random number r and the current value of y :

$$\text{if}(r.<.1/3) \ y_{new} = (1+2y)/3 \ \text{or} \ \text{if}(r.>.1/3) \ y_{new} = y/3$$

The righthand side of **Figure 3** illustrates the strange-attractor character of numerical solutions of this confined walk problem. The Confined Walk fractal at the right is related to

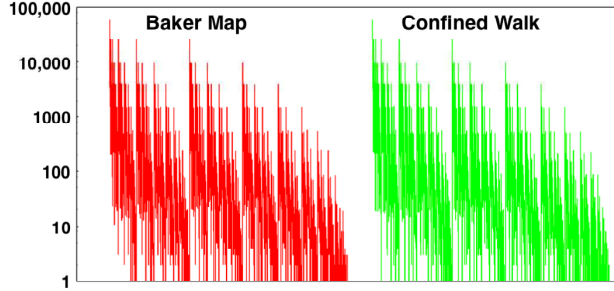


FIG. 7: Comparison of the y coordinate distribution of the Baker Map in the unit square converted from (q, p) with the Confined Walk distribution obtained using the FORTRAN random-number generator `random_number(r)`. The Map and Walk data, one million points for each, have been collected here and displayed in $2187 = 3^7$ bins of width 3^{-7} .

the Baker Map fractal at the left by a 45-degree counterclockwise rotation. Evidently, due to the exponential growth in the walk’s horizontal x direction that distribution is random and can be modelled by a good random-number generator. In the y direction the distribution is a self-similar fractal, repeating in an infinite set of bands with each band smaller than its predecessor by a factor of $(2/3)$ and including one-third as many points.

Figures 3 and 7 compare the distributions from one million iterations of the two-dimensional Baker Map with those from the same number of iterations applied to the confined walk. In **Figure 7** the unit-interval y values have been “binned” into $3^7 = 2187$ bins of equal width, $\delta = 1/2187$. Initially the doubling of density with steps to the bottom third of the square and halving with steps to the upper two thirds gives rise to probability density steps of factors of four. Later, in the steady state and visible in the plot where the bin probabilities are plotted on a logarithmic scale spanning 16 e-foldings, the regular steps stand out in the lefthand 3-based binnings but are less distinct in the righthand 4-based ones. This difference, along with the continual increase in e-foldings with iterations, suggests the possibility of convergence difficulties in characterizing the resultant fractal.

The only singularity in the linear Baker Map is the border line separating the red and white regions:

$$q - p = -\sqrt{(2/9)} \text{ Baker Map} \longleftrightarrow x = (1/3) \text{ Random Walk}$$

Evidently this measure-zero set of singular points is enough to generate the everywhere-singular fractal distribution of the analytic “ $\{ y \}$ ” and the computational “ $\{ \mathbf{y} \}$ ”. Let us consider further details of the latter set next.

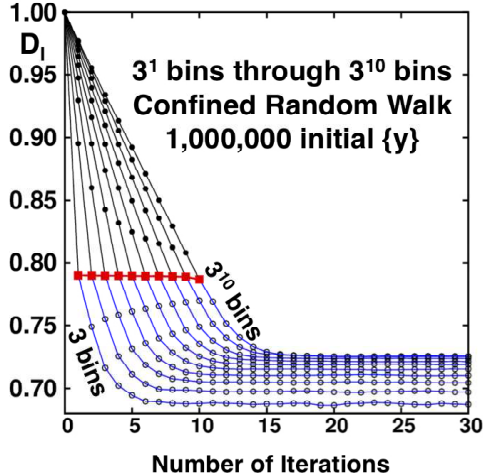


FIG. 8: The information dimensions D_I of the developing random-walk fractal as ten functions of the number of iterations. The number of bins characterizing each curve varies from 3^1 to 3^{10} for each of thirty iterations. Each point corresponds to an averaged D_I from one million equally-spaced initial conditions on the unit interval $0 < y < 1$. In the limiting special cases (shown as red squares) that the number of iterations is equal to the logarithm, base-3, of the number of bins, the information dimension follows from Farmer's analysis¹¹, $[(2/3) \ln(2/3) + (1/3) \ln(1/6)] / \ln(1/3) = 0.78967$. When the number of iterations approaches infinity ahead of the number of bins, the dimensionality is substantially lower, $D_I \simeq 0.7415$ rather than the Kaplan-Yorke conjectured value (based on the Baker-Map Lyapunov exponents) 0.7337.

VII. NONUNIFORM CONVERGENCE OF THE INFORMATION DIMENSIONS

The definition of the information dimension $D_I(\delta)$ for a set of points describes the dependence of the probability density of points on the size of the sampling bins, δ . Although other fractal dimensions can and have been defined and studied, the information dimension is uniquely significant. Unlike the correlation dimension D_I is unchanged by simple coordinate transformations¹⁴.

To seek uniqueness both the number of bins and the number of points per bin must approach infinity in averaging the bin probabilities: $D_I = \langle \ln(\text{prob}) \rangle / \ln(\delta)$. To visualize taking this limit we illustrate the result of iterating a set of one million equally-spaced initial points on confined random walks: $0 < \{y_i(t)\} < 1$. We explore thirty iterations: $0 < t < 31$. The confined random-walk iterations are governed by the output of the FORTRAN random number generator `random_number(r)`. The dimensionality data are analyzed here using 3^n

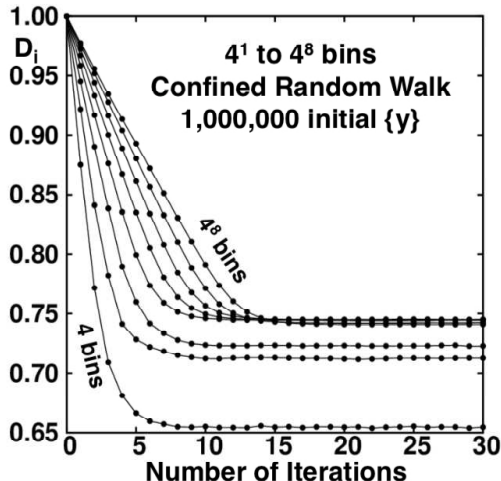


FIG. 9: The information dimension D_I of the developing random-walk fractal as a function of the numbers of bins and iterations. The number of bins varies from 4^1 to 4^8 for thirty iterations. As in **Figure 7** each point corresponds to D_I for one of the ten samples of one million initial conditions.

bins, with n varying from 0 to 10. The finest grid has $3^{10} = 59,049$ bins of equal width $\delta = 1/59049$. By combining the contents of 3, or 9, or 27, or ... contiguous bins the entire set of 30 stepwise information dimensions for the ten binnings choices can be obtained from a single run. The apparent information dimensions for the 300 problems (thirty iterations with ten bin sizes) are plotted as the ten lines shown in **Figure 8**.

The Baker-Map function, $y = [(q + p)/\sqrt{2} + 1]/2$ provides the same fractal as does the confined walk, penetrating, in both cases, to a scale smaller by a factor 3 with each iteration. For this reason powers of $(1/3)$ are the “natural” bin sizes for analyzing the Baker-Map function^{11,12} and the confined walk $0 < y < 1$. Although reciprocal bin widths which are powers of 3 are “natural” for the Baker Map and its confined walk analog, an embarrassing variety of choices is possible. As an example bin widths which are the first eight powers of 4 (a subset of bin widths which are powers of 2) provide the information dimension estimates shown in **Figure 9**. For additional examples see Reference 14. The totality of these results is paradoxical because they indicate a limiting information dimension of 0.741_5 from the series of widths $(1/3)^n$ and a *different* limit, 0.7337 , from the series of widths $(1/4)^n$. This difference suggests a persistent difference of distributions in the limiting case(s) $\delta \rightarrow 0$. This nonuniform convergence caught us completely by surprise.

The dependence of the limiting information dimension on the bin-width power law, giving either 0.741_5 or 0.7337 , suggests a look at the distributions themselves. As the limiting

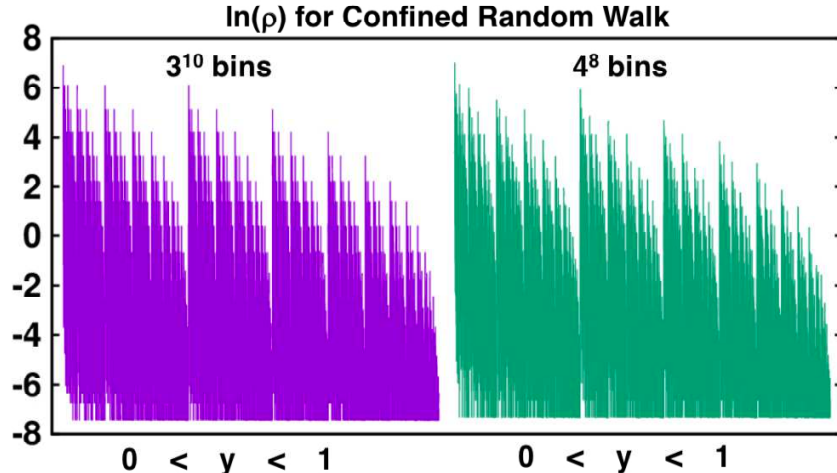


FIG. 10: Fractal probability densities for confined walks with bin sizes $\delta = 3^{-10}$ and 4^{-8} . For both bin sizes $\int_0^1 \rho(y) dy = 1$. 100 million iterations of the map were used for the point set that was analyzed with both these choices of binning.

case(s) are singular everywhere, we arbitrarily choose to compare probability densities for both 3^{10} and 4^8 bins in **Figure 10**. Both simulations include exactly the same set of 100,000,000 iterations. The density steps with 3^{10} bins are markedly sharper than those with 4^8 and the details of the boundaries between vertical strips are likewise better defined for the finer (65536 rather than 59049 bins) mesh.

A clearer picture of the binning dependence follows from the cumulative distributions of density and information, shown for the same data used in **Figure 10**. **Figure 11** shows both the density and the information dimension as cumulative sums for two pairs of similar binnings, $(1/3)^5 \sim (1/2)^8$ and $(1/3)^7 \sim (1/2)^{11}$. Because the underlying data are identical the densities always agree, within one bin width. The information dimensions are quite different with powers of 2 both giving $D_I = 0.745$, significantly greater than $D_I = 0.715$ and 0.725 for the “natural choice” of powers of three, 243 and 2187 bins. Numerical work suggests that the difference persists even to infinitesimal bin widths.

VIII. SUMMARY AND THE 2021 SNOOK PRIZES

The finding that nonequilibrium steady states with time-reversible motion equations generate repeller-attractor pairs in phase space has been explored here for two simple models, the Confined Walk and the Baker Map. These models, with one- and two-dimensional phase

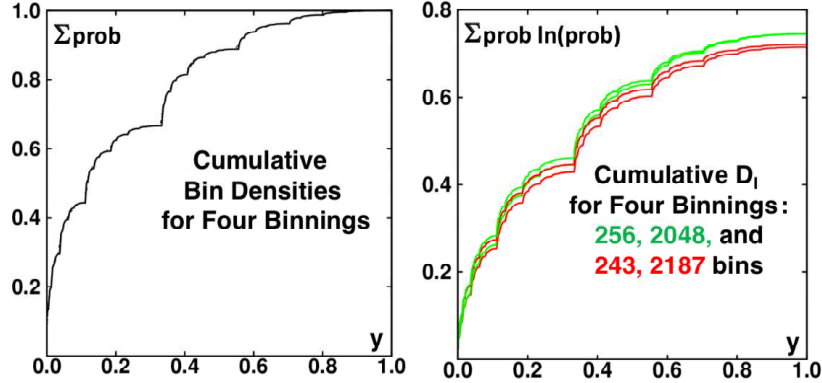


FIG. 11: Cumulative densities and information dimensions are compared for bin widths (from bottom to top at the right) of $(1/3)^5$, $(1/3)^7$, $(1/2)^{11}$, $(1/2)^8$. The information dimensions for much narrower bins suggest different limiting dimensionalities for the two bin families.

spaces, are simpler than the continuous flows illustrating chaos^{9,10}. The two model systems reveal the details of the singular loss of phase volume resulting in these interesting fractal distributions. Flows, with differential equations rather than maps, require three phase-space dimensions for chaos.

The maps have shown us that nonequilibrium states are rare, occupying only fractional dimensional portions of phase space. Although the time-symmetry of the motion equations guarantees that there is a mirror-image $p \rightarrow -p$ solution of the motion equations our investigation shows that the dissipative states form an attractor, with a negative Lyapunov-exponent sum. The attractor is a fractional-dimensional stable sink relative to the two-dimensional equilibrium phase space. The paradoxical time-reversed repellor states have positive Lyapunov-exponent sums and are wholly unstable and irreversible.

The structures of nonequilibrium steady-state phase space flows are qualitatively different to those of Gibbs' equilibrium ensembles. The steady state flows are directed *from* repellors *to* attractors. The barrier to reversal is exponential. Loschmidt's reversed states are nearly unobservable, like the attractor states so rare that they never turn up for long. Zermélo's recurring states are simply typical non-paradoxical dissipative states on stable attractors occupying a fractional-dimensional zero-volume portions of their phase spaces. Thus nonequilibrium systems are qualitatively different to Gibbs' space-filling distributions of points. It is interesting to note that the nonequilibrium fractals have the form of periodic orbits which cannot be reversed. Even for the simple Baker Map only about ten percent of the timesteps can be reversed precisely. The Lyapunov instability going backward in time

changes sign, from attractive to repulsive with the Lyapunov instability offset by convergence going forward but completely uncontrolled backward despite the time-reversibility of the equations of motion.

Detailed characterizations of the fractals found in the Walk and Map problems have revealed an unsettling nonuniformity of convergence. Different approaches to the information dimensions of the models [$\delta = (1/3)^n$ and $\delta = (1/4)^n$, for instance] give different results¹¹!

We believe that further study of these fractals is warranted. As an inducement the 2021 Snook Prize problem seeks to shed light on the information dimension of the fractals, 1.7337 *versus* 1.741₅ for the Baker Map, equivalent to 0.7337 *versus* 0.741₅ for the Confined Walk problem. Straightforward binning calculations, along the lines of **Figures 8 and 9** , give histogram probabilities { $\text{Prob}(\delta)$ } which can then be analyzed for a bin-width dependent information dimension:

$$D_I(\delta) = \langle \ln(\text{Prob}[\delta]) \rangle / \ln(\delta) .$$

Computations of $D_I(\delta)$ for small bin sizes appear to lead to three different estimates for the $\delta \rightarrow 0$ limiting “information dimension”! Evidently *the* information dimension¹¹⁻¹⁴ of these maps (in the limit that the bin-width δ vanishes) is ill-defined, an interesting example of nonuniform convergence. For further information on the 2021 Snook Prizes, one thousand United States dollars, see the articles available free at CMST.eu, the web site of the open-access journal Computational Methods in Science and Technology.

-
- ¹ W. G. Hoover and H. A. Posch, “Chaos and Irreversibility in Simple Model Systems”, *Chaos* **8**, 366-373 (1998).
 - ² S. Tasaki, T. Gilbert, and J. R. Dorfman, “An Analytical Construction of the SRB Measures for Baker-Type Maps”, *Chaos* **8**, 424-443 (1998).
 - ³ J. Kumičák, “Irreversibility in a Simple Reversible Model”, *Physical Review E* **71**, 016115 (2005).
 - ⁴ W. G. Hoover and C. G. Hoover, *Time Reversibility, Computer Simulation, Algorithms, Chaos*, 2nd Edition, (World Scientific, Singapore, 2012).
 - ⁵ W. G. Hoover and C. G. Hoover, *Microscopic and Macroscopic Simulation Techniques: Kharagpur Lectures*, (World Scientific, Singapore, 2018).

- ⁶ S. Nosé, “A Unified Formulation of the Constant Temperature Molecular Dynamics Methods”, *The Journal of Chemical Physics* **81**, 511-519 (1984).
- ⁷ S. Nosé, “A Molecular Dynamics Method for Simulations in the Canonical Ensemble”, *Molecular Physics* **52**, 255-268 (1984).
- ⁸ W. G. Hoover, “Canonical Dynamics. Equilibrium Phase-Space Distributions”, *Physical Review A* **31**, 1695-1697 (1985).
- ⁹ B. L. Holian, W. G. Hoover, and H. A. Posch, “Resolution of Loschmidt’s Paradox: The Origin of Irreversible Behavior in Reversible Atomistic Dynamics”, *Physical Review Letters* **59**, 10-13 (1987).
- ¹⁰ W. G. Hoover, H. A. Posch, B. L. Holian, M. J. Gillan, M. Mareschal, and C. Massobrio, “Dissipative Irreversibility from Nosé’s Reversible Mechanics”, *Molecular Simulation* **1**, 79-86 (1987).
- ¹¹ W. G. Hoover and C. G. Hoover, “2020 Ian Snook Prize Problem: Three Routes to the Information Dimensions for One-Dimensional Stochastic Random Walks and Their Equivalent Two-Dimensional Baker Maps”, *Computational Methods in Science and Technology* **25**, 153-159 (2019). arXiv 1910.12642.
- ¹² J. D. Farmer, “Information Dimension and the Probabilistic Structure of Chaos”, *Zeitschrift für Naturforschung* **37a**, 1304-1325 (1982).
- ¹³ W. G. Hoover and C. G. Hoover, “Random Walk Equivalence to the Compressible Baker Map and the Kaplan-Yorke Approximation to Its Information Dimension”, arXiv 1909.04526.
- ¹⁴ E. Ott, W. D. Withers, and J. A. Yorke, “Is the Dimension of Chaotic Attractors Invariant Under Coordinate Changes?”, *Journal of Statistical Physics* **36**, 687-697 (1984).